ACS APPLIED NANO MATERIALS

www.acsanm.org Article

Wavelength-Dependent Plasmonic Photobleaching of Dye Molecules by Large-Area Au Nanostripe Arrays

Matteo Barelli, Giulio Ferrando, Maria Caterina Giordano, and Francesco Buatier de Mongeot*

Cite This: *ACS Appl. Nano Mater.* 2022, 5, 3470−3479 Read Online

ACCESS | Metrics & More | Article Recommendations | Supporting Information

ABSTRACT: The development of clean light-harvesting platforms and technologies is crucial in view of the urgent energy and environmental global challenges. Plasmonic nanoparticles show great promise in light-harvesting applications, but their fabrication is typically constrained to small-area laboratory-scale methods or to highly polluting wet chemistry approaches that are not suitable for environmental applications such as waste water recycling. In this work, we propose a self-organized method to fabricate large-area (cm^2, industrially scalable up to m^2) plasmonic templates. Ordered Au nanostripe arrays supported on cheap, nontoxic soda-lime glass substrates are prepared, showing a tunable plasmonic response. We demonstrate enhanced photochemical reactivity and photobleaching of highly polluting methylene blue molecules promoted by this self-organized plasmonic platform. We investigate this effect by tailoring the spectral overlap between the molecule absorption band and the plasmon resonance and by tuning the monochromatized excitation wavelength. This kind of study is completely lacking in the literature for big molecules with optical absorption bands in the visible range. We demonstrate the dominant role of plasmon-enhanced near-field optical effects over hot-carrier injection in amplifying photodissociation of colored dye molecules, thus paving the way to the engineering and optimization of light-harvesting platforms for waste water treatment, dye molecule sensing devices, and a broad range of other light-harvesting applications.

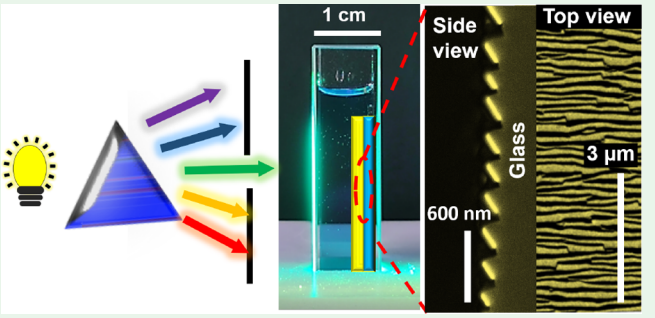

KEYWORDS: *light harvesting, plasmon-enhanced photocatalysis, hot electrons, solid-state large-area nanofabrication*

INTRODUCTION

Subwavelength confinement and manipulation of light at the nanoscale have witnessed an impressive development over the last decades.[1−4] In particular, plasmonic resonances sustained by noble metal nanostructures in the visible and near infrared spectral ranges, a well-known phenomenon extensively investigated by classical electromagnetic theory, started to gain an ever increasing deal of attention because of the development of new and more powerful technological means of nanofabrication and characterization of nanomaterials.[5,6] Resonant plasmonic nanostructures enable the strong confinement of optical fields in subwavelength volumes along with enhanced light scattering and absorption cross sections, all crucial features exploited in a huge range of nanophotonics and optoelectronics technological applications and research fields.[7−15] Another interesting possibility has more recently been addressed for exploiting electronic losses in metal nanoparticles, which were traditionally perceived as crucial liability of this class of nanomaterials compared to their dielectric counterparts.[16,17] Indeed, plasmonic quasi-particles excited in a metal due to resonant light absorption can also decay nonradiatively promoting resonant electronic excitation to a higher, athermal energy state. These *hot electrons* in a non-Fermi distribution very quickly relax back in a cascade of electron−electron, electron−phonon, and phonon−phonon processes, ultimately leading to the heating of the metal lattice, but they can also be extracted outside of the metal itself.[18,19] In particular, one of the fields where the light-energy harvesting properties and hot-carrier extraction of plasmonic nanoparticles are rising the higher interest is surface-enhanced photocatalysis. The latter represents a crucial area of research in view of a reduction of the massive environmental toll of the chemical industry as the sector is the world's largest industrial energy consumer.[20−23] Critical environmental hazards such as water pollution must be faced by developing more energy-efficient processes driven by photons rather than heat, with possibly new and unique selectivity, by harvesting free and clean sunlight with large-area nontoxic solid-state plasmonic platforms. In this context, we highlight that traditional high-

Received: November 29, 2021
Accepted: March 1, 2022
Published: March 9, 2022

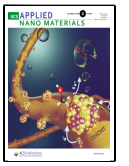

https://doi.org/10.1021/acsanm.1c04087
ACS Appl. Nano Mater. 2022, 5, 3470−3479

band-gap semiconductor photocatalysts such as TiO_2 and polluting wet chemistry nanoparticle solutions do not represent a suitable alternative.[24]

A whole range of different approaches have been explored and studied in surface-enhanced plasmonic photocatalysis. Enhanced photocatalysis by metallic nanoparticles has been observed in a huge range of photochemical reactions going from the oxidation of several chemical species such as for HCHO, CO, NH_3 to ethylene epoxidation,[22] CO_2 reduction,[25] localized growth of molecular or metallic structures,[26−28] H_2 dissociation,[29] water splitting,[30] Suzuki coupling reactions,[31] decomposition of organic dyes,[32] solar desalination,[33] and many more. Various mechanisms have been proposed and discussed which differ considerably between each other and from a particular reaction to the other. An important effect is played by near-field amplification in the proximity of resonant plasmonic nanoparticles,[11,12] which can play an important role in the photocatalysis of a crucial class of environmentally hazardous analytes such as highly polluting colored dye molecules, but the former so far has been poorly studied in sight of this application.[22] This effect can boost light−matter interaction in molecules absorbed or immersed in the near-field region surrounding the nanoantennas when a spectral overlap is obtained between the plasmonic resonance of the photocatalyst, the wavelength of the pump light source, and the optoelectronic properties of the analytes. This phenomenon is essentially analogous to the well-known electromagnetic field enhancement responsible for surface-enhanced Raman spectroscopy (SERS).[7,34] In the case of plasmonic hot carriers, their injection from the resonant metal nanoparticle surface into the typically small and transparent absorbed molecule highest occupied molecular orbital/lowest unoccupied molecular orbital (LUMO) has been identified as mainly responsible for the observed enhanced photochemical activity in many reported literature studies.[22] Also promotion of the formation of very reactive radical species such as $OH^{\bullet}$ and oxygen singlet by hot-electron injection from metallic nanoparticles into aqueous media has been identified as a relevant effect.[35−37] In addition, more complex strategies have been explored involving the use of heterostructures rather than bare monometallic nanostructures,[22,35,36,38−40] such as bimetallic nanoparticles,[31,41] hybrid optical modes in near-field coupled structures,[42,43] and metal/semiconductor heterojunctions exploiting the Schottky junction at the interface between the two materials for hot-carrier injection.[18,44−46]

Unfortunately, most of the described approaches rely on laboratory-scale, small-area, lithographic top-down fabrication techniques or highly polluting wet-chemistry-based methods that are not suitable for a crucial class of real-world applications such as wastewater purification. There is the crucial need for the development of cost-effective, bottom-up approaches enabling the fabrication of large-area, nontoxic, efficient plasmonic photocatalytic platforms. Regrettably, to our knowledge, all studies involving the plasmon-enhanced photobleaching of organic dyes rely on broadband illumination, thus lacking a more detailed investigation of the interplay between the optical properties of the plasmonic nanostructures and the analytes. Indeed, all the sparse existing wavelength-dependent plasmon-assisted photocatalysis studies employing monochromatic light sources involve small transparent molecules, for which the near-field enhancement effect is not expected to be dominant, because of the spectral mismatch between the optical absorption band of the catalyst and the analytes.

In this work, we demonstrate the enhanced photobleaching of methylene blue (MB), one of the most polluting organic molecules commonly used in the textile industry, by large-area arrays of anisotropic gold nanostripes (NSs) endowed with a tunable plasmonic response. These nanoantennas are firmly confined on top of cheap, nontoxic soda-lime glass nanorippled templates fabricated by an innovative, scalable technique based on ion beam sputtering (IBS).[47] Employing a wavelength-selected excitation, we show the possibility to strongly enhance the efficiency of the photobleaching process via resonant plasmonic near-field confinement. In analogy with the signal amplification induced in SERS,[7,34,48,49] here we highlight the crucial role of plasmonic near-field in boosting the resonant electronic transitions of the dye molecules. We believe that this self-organized nanostructured surface based on engineered nanoantennas promoting resonant plasmon-enhanced photobleaching of highly polluting colored dye molecules could have an important impact in various applications ranging from waste water remediation to energy harvesting and storage.

RESULTS AND DISCUSSION

Large-area nanopatterns at surfaces can be obtained in a scalable and cost-effective way recurring to self-organization phenomena which create regular geometric and/or temporal patterns and decrease the entropy locally, in contrast to random processes. Observations of self-organized pattern formation are reported both for growth (deposition) at surfaces or for the complementary process during ion erosion, and the time evolution of the surface profile can be theoretically described recurring to continuum models based on stochastic nonlinear equations.[50−52] The essential physics behind the pattern formation process can be highlighted already in the linear approximation of the stochastic equations, such as the Bradley−Harper model: competition between the stochastic arrival of ions (which destabilize the surface profile inducing roughening) and mass redistribution via thermally and ion-activated diffusion (which reduce the height profile) leads to the formation of regular ripple patterns.[53]

The experimental conditions employed in this experiment are chosen so to exploit a further thermodynamic driving force (ion-induced wrinkling instability) to speed up the kinetics of pattern formation.[47] A soda-lime glass ($2 \times 2 \times 0.2$ cm^3) is irradiated with a defocused low energy (800 eV) argon ion beam at an incidence angle $\theta = -30°$ with respect to the glass surface normal, while the temperature of the copper sample holder is kept at a fixed temperature of about 680 K (see Methods for details). The defocused IBS process chisels a remarkably ordered self-organized quasi-one-dimensional (1D) morphology all over the macroscopic glass surface, with the nanoripples long axis orthogonal to the ion beam direction (Figure 1a). The ripples are endowed with a prominent vertical dynamic of about 60 nm (Figure 1b), a periodicity of about 200 nm evaluated from the autocorrelation of atomic force microscopy (AFM) measurements (see Figure S1), and length exceeding several micrometers. The nanoripples show an asymmetric saw-tooth profile (Figure 1c) with the facets opposing the ion beam direction distinguished by long hillsides and a sharply defined slope distribution peaked at about +35° (Figure 1c).[54] The facets directly facing the ion beam develop shorter and steeper hillsides instead, with a shallow slope distribution peak at about −45° (Figure 1c). These results are

https://doi.org/10.1021/acsanm.1c04087
ACS Appl. Nano Mater. 2022, 5, 3470−3479

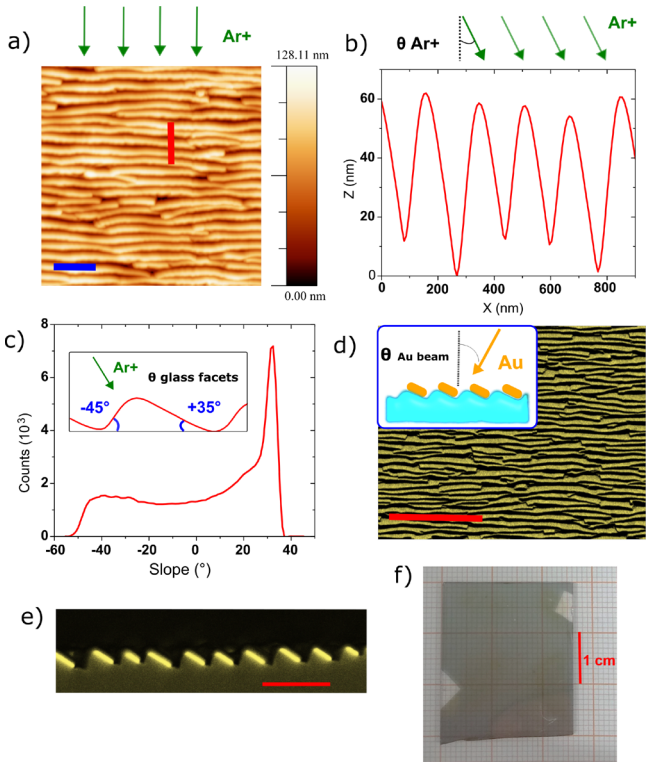

Figure 1. (a) AFM topography of the nanorippled glass template. The blue scale bar corresponds to 800 nm. (b) Extracted AFM line profile corresponding to the red bar in panel (a). (c) Histogram of the ripple ridge slope distribution. The inset shows a sketch of the ripple geometry with respect to the incident Ar + beam direction. (d) Rendered top-view scanning electron microscopy (SEM) image acquired in the backscattered electrons channel of the Au NSs confined on the nanorippled glass template. The red scale bar is 3 μm long. The insets provide a sketch of the sample cross section and thermal Au deposition geometry. (e) Rendered SEM image acquired in the backscattered electron channel of the cross section of the Au NSs supported on the nanorippled glass template. The red scale bar is 600 nm long. (f) Macroscopic picture of a sample before the cut to fit in the 1 × 1 cm^2 cuvette.

in striking contrast with IBS experiments performed at room temperature on the same glass substrates and in general on amorphous, insulating substrates, which typically yield shallow, low-aspect ratio (AR), disordered ripples which are unsuitable for subsequent technologically relevant surface functionalization.[55,56] The observed enhancement of the ripples' vertical dynamic and morphology is attributed to a nanoscale wrinkling instability, activated when the sample temperature approaches the glass transition threshold (~550 °C), and the enhancement of mass transport contributes to nanopattern formation via relaxation of the ion-induced surface stress.[47] Very recently, some of the authors also demonstrated how the shape and slopes of the nanoripples asymmetric profile can be tailored by tuning the ion beam incident angle, configuring high-AR, well-ordered, quasi-1D nanoripple arrays. This degree of freedom enables the engineering of asymmetric nanofacets characterized by a controlled width and local tilt.[47,54] These nanostructures are supported on cheap and transparent substrates and are homogeneous over a large area (cm^2 scale) (see Figure 1f), acting as ideal templates for the confinement of nanoantenna arrays and nanorippled plasmonic thin films, with peculiar optoelectronic and biosensing functionalities.[49,54,57−59] Provided the controlled morphology of the glass template, easy tailoring of the shape of the nanoantennas can be achieved by controlling the metal incidence angle and/or the metal thickness during the thermal growth.

In this work, we exploit the nanorippled glass templates for the self-organized confinement of quasi-1D arrays based on tilted Au NSs. Their shape has been engineered to explore their role in the photocatalysis of MB molecules. Au NSs are confined selectively on either the long or short facets of the nanorippled profile by exploiting shadowing effects during deposition of metal atoms at grazing angles (Figure 1d,e). The thickness h of the stripes is precisely controlled by the sublimated Au dose, while the width w and the tilt of the stripes are a function of the local Au beam angle of incidence with respect to the ripple ridges, showing a size distribution which directly depends on the underlying self-organized nanorippled template (see the Methods section for details). In particular, we fabricated three different samples characterized by different NS tilts and aspect ratios, the latter defined as AR = h/w. In Figure 2d−f, we show cross-section schemes

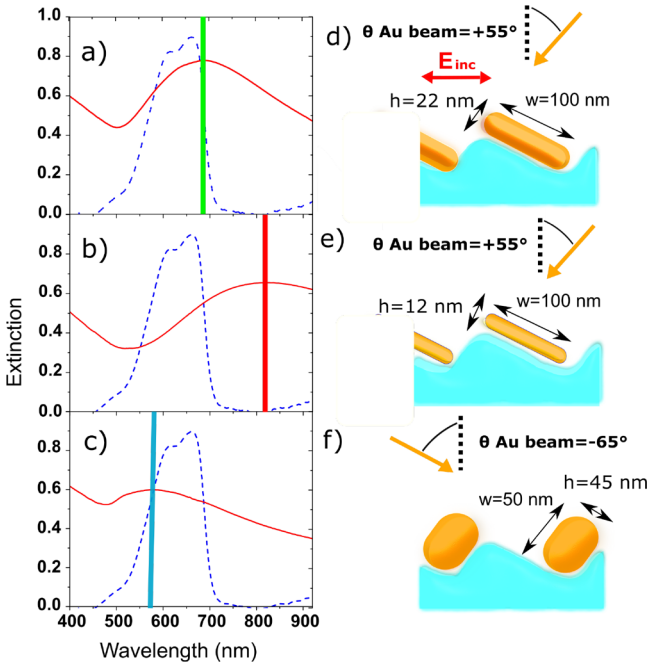

Figure 2. (a−c) Extinction spectra of samples A, B, and C, respectively (solid red traces), normalized to the ones of bare glasses in MB solution. Dashed blue traces are MB solutions' extinction spectra for all three panels. Colored vertical bars underline the Au NSs LSPR peak wavelength. (d−f) Fabrication and morphological feature cross-section sketch of the Au NSs of samples A, B, and C respectively along with the orientation of the electric field polarization employed in the extinction measurements (red arrow in panel d).

of the fabrication processes evidencing the morphological features of the NSs arrays. In Figure 2a−c (dashed blue traces), we report normal-incidence unpolarized extinction spectra of bare MB solutions overlapped with analogous measurements performed for the three samples (solid red traces) immersed in MB solutions for TM polarization (spectra are normalized to isolate the Au NSs contribution, see Figure S2), that is, with the electric field oscillating along the subwavelength cross section of the Au NSs and orthogonally to their elongation

https://doi.org/10.1021/acsanm.1c04087
ACS Appl. Nano Mater. 2022, 5, 3470−3479

direction (see the sketch in Figure 2d and Methods for details). For this polarization configuration, localized surface plasmon resonance (LSPR) is excited over the Au NSs. A detailed quantitative modeling of the LSP resonant wavelength requires numerical FEM calculations (see, e.g., ref 59 for similar Au NSs). It is well known from seminal analytical calculations that, as a rule of thumb, decreasing the nanostructure AR compared to a symmetrical nanostructure one obtains a redshift of the LSPR and vice versa.[5,60] The versatility of our large-area nanofabrication approach allows us to engineer the geometrical features and thus to spectrally tune the LSPR of the different samples by controlling simple experimental parameters such as the metal thermal deposition angle and dose, as the LSPR peak wavelength is a function of the nanoparticle shape and size.[60] This tunability enables investigating the effects of varying degrees of spectral overlap between the different LSPR of the three Au NSs samples and the MB molecule absorption peak; in the plasmon-enhanced photobleaching experiments this will be described further ahead in the discussion.

In particular, for sample A we confined Au NSs on the +35° tilted long facets of the nanorippled template (Figure 2d), the thickness h of the stripes reads 22 nm while their average width w is 100 nm; thus the stripe aspect ratio equals AR = 0.22. The clear extinction peak at 690 nm (Figure 2a, evidenced by the blue bar) is associated with the excitation of a LSPR over the Au NSs section. For sample B (Figure 2e), the same deposition geometry is maintained but thinner, h = 12 nm, stripes are confined and thus the AR of the Au NSs decreases with respect to sample A to AR = 0.12. The LSPR peak of sample B is associated with the extinction peak at 820 nm (Figure 2b, evidenced by the red bar), showing a remarkable 130 nm redshift compared to the LSPR of sample A, in accordance with theoretical arguments expecting a nonlinear LSPR redshift for elliptical particles of decreasing AR in this incident electric field polarization configuration.[60] The LSPR extinction intensity drops because of the decreased Au thickness with respect to sample A. For sample C, we grow the Au NSs on the −45° tilted short facets (Figure 2f). The structures are 45 nm thick and show an average width of 80 nm; they thus possess a higher AR = 0.56, which translates in a blueshifted resonance peaked at 560 nm (Figure 2c, evidenced by the blue bar). For sample C, because the effective area of the glass surface covered by Au NSs is smaller than that for samples A and B we do not observe an increase in LSPR extinction. Additionally, because of the relevant tilt of the NSs axis with respect to the horizontal plane, the electrical field vector can also couple efficiently with the LSP resonance along the short axis of the Au NSs cross section, which is blueshifted and contributes to the overall broadening of the extinction spectrum compared with the samples of Figure 2a,b.[59,60] As expected, the measurements performed in MB show a broadening and a redshift of the LSPR compared to measurements performed in air, because of the increase of the surrounding medium dielectric constant (see Figure S2 for measurements in air).

Sample A is cut to fit in a 1 × 1 cm^2 square section cuvette filled with a 1.3 × 10^{-5} M MB solution and illuminated by a linearly polarized monochromatized Xenon lamp source, after a complete MB absorption−desorption equilibrium is reached by the sample and cuvette surfaces (see Figure S3 and Methods for details). The sample glass flat side adheres to the cuvette internal wall opposing the light beam, while the sample nanopatterned side functionalized with the Au NSs directly faces the source, which is polarized in TM configuration to excite LSPR on the plasmonic nanostructures (Figures 3a and S4). The absorbance of the MB solution is monitored at regular time intervals with a simple optical transmission setup, along with the one of a reference solution which is exposed to light excitation without a sample inside it. Experiments are performed for different light wavelengths at a constant power flux of 2 mW cm^{-2}, as measured on the cuvette surface (see Methods for experimental details), which compared to the AM1.5 g reference solar irradiance approximately corresponds to a 10% fraction. In Figure 3b, we show the evolution of the normalized concentration of the MB solution containing sample A (red triangles), compared to the reference MB solution (blue dots) with increasing photon dose. Both the solutions were exposed to a monochromatic light source tuned at the wavelength λ = 680 nm, which is resonant with both the LSPR of sample A and MB absorption band (Figure 2a). The plot of Figure 3b clearly highlights that the presence of Au NSs strongly speeds up the MB photobleaching process compared to the case of the bare solution. Experiments were carried out for different excitation wavelengths, enabling the calculation of the kinetic constant κ_{sample} and $\kappa_{reference}$ employing the first-order reaction kinetic law $[C] = [C_0]e^{-kt61}$ where C is the MB concentration as a function of time, C_0 is the initial MB concentration, and t is the exposure time, for both the sample and the reference solution, plotted in Figure 3c as a function of the excitation wavelength (see Methods). In the case of bare reference MB solutions, a clear direct proportionality between

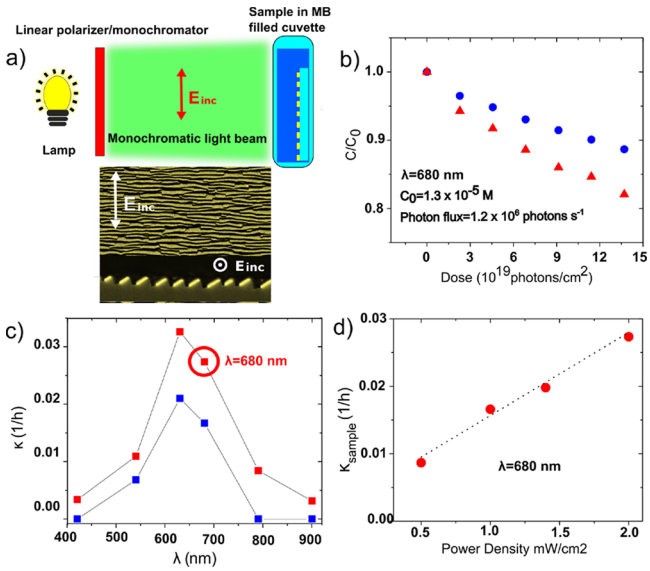

Figure 3. (a) In the top part of the panel, we show a cross-section sketch of the experimental setup. The bottom part of the panel shows a SEM image of the Au NSs to clarify the polarization of the incoming light beam (TM polarization) with respect to the Au NSs orientation in both top (upper image) and cross-sectional views (lower image). (b) Normalized concentration of the bare MB solution (blue dots) and sample containing solution (red triangles) as a function of photon dose (pump source wavelength λ = 680 nm). (c) Kinetic constants of bare MB solution $\kappa_{reference}$ (blue squares) and sample containing solution κ_{sample} (red squares) as a function of the pump source wavelength λ. The red circle highlights the experimental point corresponding to λ = 680 nm. (d) κ_{sample} values at the constant pump wavelength λ = 680 nm changing the power density illuminating the MB-filled cuvette containing the sample.

https://doi.org/10.1021/acsanm.1c04087
ACS Appl. Nano Mater. 2022, 5, 3470−3479

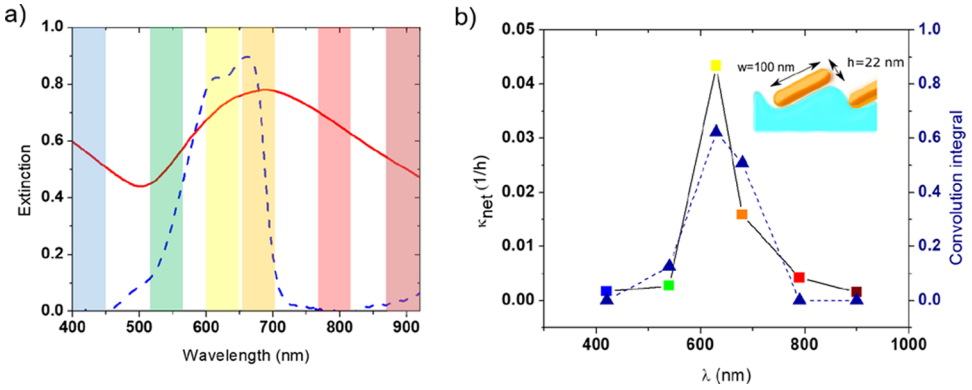

Figure 4. (a) Extinction spectra of sample A Au NSs (solid red trace) and of MB bare solution (dashed blue curve). (b) Normalized κ_{net} to the source power density reaching the Au NSs (colored squares) and convolution integral value (blue triangles) as a function of source wavelength λ for sample A.

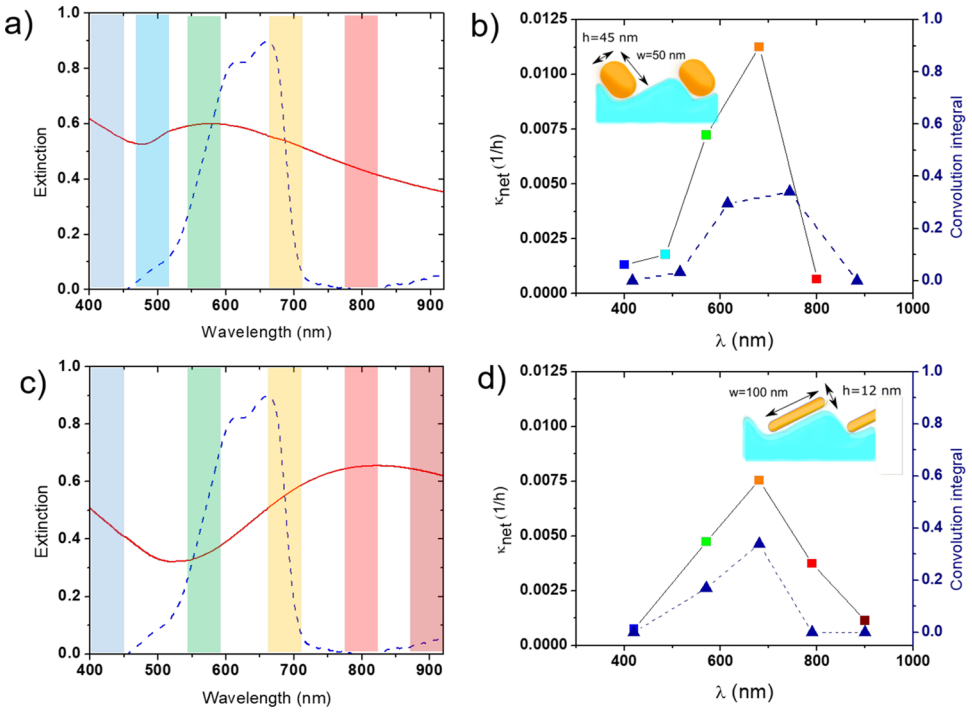

Figure 5. (a,c) Extinction spectra of sample C and B Au NSs (solid red traces) and of MB bare solution (dashed blue curve), respectively. (b,d) Normalized κ_{net} to the source power density reaching the Au NSs (colored squares) and convolution integral value (blue triangles) as a function of source wavelength λ for samples C and B, respectively.

the kinetic constant value $\kappa_{reference}$ (Figure 3c, blue squares) and the molecule absorption band strength at a particular λ is observed, in good agreement with previous literature.[62] The reader can refer to Figure S5 for a more extended set of experiments performed on MB solutions which explores this correlation in more detail. Because of the low photon exposure doses employed in the experiments, the exponential decrease in MB concentration with time (first-order chemical kinetics) can be analytically approximated by a linear decay $[C] = [C_0](1 - kt)$. The MB solution containing the sample is characterized by a faster MB photobleaching reaction for all the employed excitation wavelengths, as highlighted by the larger kinetic constants κ_{sample} (Figure 3c, red squares). We observe a sample-related enhancement of the reaction kinetic constant κ_{sample} compared to $\kappa_{reference}$ both at a source wavelength of 400 and 800 nm, where the MB solution is completely transparent and no direct photoreaction takes place in the bare MB solution. The latter observation clearly points to the role of hot electrons injected from the Au NSs, possibly causing the production of highly oxidizing radical species in aqueous solution or MB reduction because of the injection of hot electrons into the molecule LUMO levels .[29,35,38] On the other side, the stronger kinetic enhancements are observed when the pump wavelength is tuned with both the particle LSPR and MB absorption band, which suggests the dominant role of plasmon-enhanced optical effects that will be highlighted in detail in the following discussion. In Figure 3d, we report κ_{sample} values obtained in experiments performed by changing the power of the light source tuned at λ = 680 nm. A clear linear trend is observed thus excluding thermal effects on the MB photobleaching enhancement because of Au NSs heating, leading to the conclusion that we are observing purely optical and hot-carrier-related effects.[22] This is in agreement

https://doi.org/10.1021/acsanm.1c04087
ACS Appl. Nano Mater. 2022, 5, 3470−3479

with the fact that the sample is excited at low surface power density, in the range of few mW/cm^2.

To investigate more in depth the role of the plasmonic nanoantennas, we measured the MB photobleaching rates on the three different Au NSs samples at varying excitation wavelength λ. In Figure 4a, we plot the extinction spectra of both sample A (solid red curve) and reference MB solution (blue dashed curve), along with the underlying colored boxes which represent the light excitation bandwidth in the different experiments. In Figure 4b, we plot a quantity that we define as $\kappa_{net} = \kappa_{sample} - \kappa_{reference}$ that is the net differential increase in the κ value for the solution containing the Au NSs sample versus the reference (a cuvette filled with MB solution but without sample) as a function of pump source wavelength λ. To obtain a quantitative comparison of the wavelength-dependent photobleaching efficiency of the Au NSs, the κ_{net} values are weighted by a coefficient proportional to the light power density which is effectively reaching the Au NSs on the sample surface, according to the geometry of the experimental cell sketched in Figure 3a assuming a reference incident power density of 1 mW/cm^2. For example, a κ_{net} value computed for an illumination λ where the solution in completely transparent (e.g., λ = 400 nm) will be multiplied by a weighting coefficient equal to 1. Instead, a κ_{net} value computed for a pump source λ where the solution absorbs 50% of light before reaching the Au NSs will be multiplied by a weighting coefficient of 2, as a halved light intensity will reach the sample compared to the previous case. To further evaluate the interaction between the plasmonic resonance and the molecular absorption in Figure 3b, we also plot a relevant quantity, that we call convolution integral parameter (blue triangles), calculated as the product of the integral averages of extinction in the Au NSs (E_{Au}) and in the MB solution (E_{MB}), both evaluated in the excitation bandwidth centered on a particular λ. Thus the convolution integral is defined as $\frac{1}{b-a} \times \int_a^b E_{Au}(\lambda)d\lambda \times \int_a^b E_{MB}(\lambda)d\lambda$, where $b - a$ is the bandwidth of the source, $\pm$ 25 nm with respect to monochromator selected λ (see Methods for details). In practice, what we call convolution integral it is the product of the mean extinction of sample and solution, integrated within the bandwidth of excitation. The higher the value of the convolution integral is, the higher the spectral overlap is between the sample LSPR extinction and molecule absorption. It quantifies the optical coupling between the two in the chosen illumination bandwidth. In Figure 4b, we can thus notice how the photocatalytic efficiency κ_{net} of the Au NSs is higher as the spectral overlap of the structure LSPR with the MB absorption is stronger. This indicates that the main mechanism responsible for the observed increase of the photobleaching rates in the presence of the Au NSs is the plasmonic near-field enhancement of molecular excitation in proximity to the resonant nanoantennas rather than a plasmonic hot-electron charge transfer process.

To further confirm the correlation between photobleaching activity and the convolution integral, we perform analogous experiments on sample B and sample C (Figure 5c,d) which possess differently tuned LSPR with respect to MB absorption spectra. For sample C (Figure 5a,b), we observe a very similar behavior compared to sample A. Again we observe a direct correlation between the photobleaching efficiency κ_{net} and the convolution integral value. It is worth noting that the maximum value of κ_{net} is now reduced to about one fourth compared to the one found for sample A, because of the partial detuning of the LSP resonance from the MB transition. Considering sample B (Figure 5c,d), the LSPR peak of the Au NSs is found at about 820 nm, well outside the spectral range of MB absorption. We again observe a direct correlation between κ_{net} and the overlap integral but, significantly, now κ_{net} is smaller when the excitation source is well tuned to the Au NSs LSPR at 800 nm compared to the maximum κ_{net} found at λ = 690 nm in correspondence to the MB extinction peak. These observations again suggest resonant field enhancement coupling between plasmonic structures and MB molecules as the dominant effect responsible for photocatalytic enhancement. Nonetheless a measurable κ_{net} value is observed for λ = 800 (Figure 5d, red square) even for a null corresponding overlap integral; as already discussed, this suggests that plasmonic hot-electron-related effects are playing a role in MB photobleaching.[39] It is also worth noting that average κ_{net} values fall to even lower figures compared to sample A and sample C. This suggests, as previously reported by other literature studies, that an accurate engineering of the size and morphology and the plasmonic nanostructures affecting the interplay between properties such as scattering, absorption, field enhancement intensity, and spatial distribution plays a crucial role in sight of efficient plasmon-enhanced photoreactivty.[63,64]

To further prove the dominant role played by field enhancement effects, we performed a set of MB photobleaching experiments with a sample analogous to sample A, adding a dielectric spacer with variable thickness on top of the Au NSs to control the degree of coupling between the MB molecules in solution and the plasmonic near field localized on the NSs. The experiments have been performed at a fixed excitation wavelength of 660 nm (maximum overlap between the sample LSPR and MB solution extinction) adding amorphous TiO_2 overlayers with increasing thickness on top of the Au NSs (see Figure 6a Methods for details of fabrication

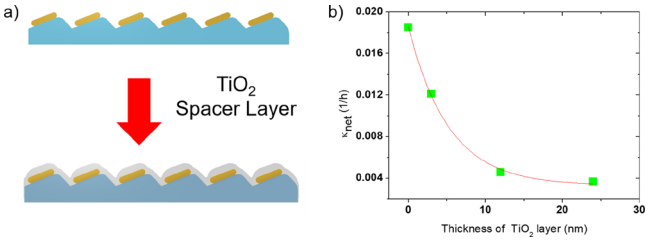

Figure 6. (a) Sketch of the TiO_2 deposition experiment and (b) MB photobleaching rate normalized with respect to uncoated Au NSs, κ_{net}, plotted as a function of TiO_2 layer thickness, at a source wavelength of 660 nm and 2 mW/cm^2 power density.

via RF magnetron sputtering). In Figure 6b, we plot the $\Delta\kappa$ measured as a function of the thickness of the TiO_2 spacer layer, finding that the reactivity follows an exponentially decaying trend as the MB molecules are separated from the Au NSs surface by the thicker spacer. We can exclude the role of hot electrons injected through the Au/TiO_2 Schottky barrier because their diffusion length in amorphous TiO_2 is limited below 3 nm, i.e, way smaller than the minimum TiO_2 coating thickness here employed.[65] Because of the geometry of our system, hot electrons injected from the Au structures recombine inside the dielectric capping layer well before reaching its surface and interacting with the MB molecules and/or aqueous solution. The relatively slow decreasing trend

https://doi.org/10.1021/acsanm.1c04087
ACS Appl. Nano Mater. 2022, 5, 3470−3479

of the MB photobleaching rate, in the range of few tens of nanometers, is instead compatible with the exponential decay of the plasmonic electromagnetic near-field confined at the Au NSs.[5]

The experiment of Figure 6b also allows excluding the role of reflectivity effects in determining the observed decreasing trend of MB photobleaching when the thickness of the TiO_2 spacer layer is increased. Indeed, as shown in Figure S7, the addition of a thin TiO_2 layer, which has a higher refractive index compared to the glass substrate, results in a slight increase of reflectivity in the order of 10% which in turn should induce a comparably weak increase of MB photobleaching during the return path of light inside the cuvette. Also, if we consider polarization-resolved reflection spectra of the Au NSs array recorded with an integrating sphere (see Figure S8), the reflectivity of the sample fluctuates about 10−20% in the spectral range explored in our experiments (from about 400 to 900 nm). This cannot explain the observed 80% variations in photobleaching efficiency with the different employed excitation wavelengths, further dismissing the relevance of far-field backreflector-like effects. To better prove this point, in Figure S9 we compare the photobleaching activity of the Au NSs sample with a flat Au reference film which acts as a backreflector at pump wavelength λ = 680 nm. We found that the kinetic constant for the Au NSs is about 1.5 times higher than the one of the back reflector. We stress that the increase in photobleaching activity of the NSs samples is observed even if thick flat Au reflectivity is 3 times higher than that of the Au NSs (see Figure S8) thus confirming and highlighting the role of plasmonic enhancement. Another important feature to be underlined is the mechanical robustness of the Au NSs arrays. The Au NSs presents no morphological variations and any kind or detachments from the glass substrate after several hours of immersion in the MB solution (see Figure S6). We attribute this improvement of film adhesion, compared to the typical weak adhesion of Au nanostructures to glass surfaces, to the sputtering treatment of the glass substrate prior to Au deposition via thermal evaporation. In perspective a further improvement of the mechanical stability of the antennas could be achieved by deposition of a thin Ti/Cr adhesion layer, at the expense of the broadening and redshift of the LSPR, as well known in the literature, because of the increased effective damping factor of the plasmonic nanostructures.[66]

CONCLUSIONS

We demonstrated the confinement of tunable plasmonic Au NSs supported over large-area, nanorippled glass templates which are nanopatterned via an innovative, cost-effective, and industrially scalable bottom-up fabrication technique based on IBS. We showed how these nontoxic, planar, solid-state tunable plasmonic platforms can be employed in the plasmon-enhanced photobleaching of MB molecules without suffering any mechanical damage in solution. We demonstrated that the efficiency of the photocatalytic process is maximized by increasing the spectral overlap between the analytes optical absorption band and the Au NSs plasmonic resonance, using a monochromatized light source and performing experiments as a function of the excitation wavelength. These experiments allowed highlighting the crucial role of the plasmonic near-field enhancement in the photocatalytic process. To further confirm this effect, we grew thick dielectric spacer layers covering the Au NSs, thus inhibiting direct injection of hot carriers from the latter into the solution, and we observed an exponential decay of the plasmon-enhanced photobleaching process with decay lengths in the range of few tens of nanometers. This result confirms the dominant effect on photobleaching of the optical plasmonic near-field tuned in resonance to the colored dye molecule absorption band. These findings pave the way to the optimization of the platform for applications such as waste water treatment where the plasmonic resonance can be easily tuned in resonance to the target molecule absorption band by tailoring the Au NSs geometry, metal composition, or architecture (e.g., magnetic modes in plasmonic dimers)[59,67] and a broad range of other light-harvesting and sensor applications.

METHODS

Sample Fabrication. A soda-lime glass (2 × 2 × 0.2 cm^3) is rinsed for 10 min in both acetone and isopropylic alcohol and put in a custom-made vacuum chamber pumped down to a pressure in the order of 10^{-6} mbar. The sample surface is then irradiated by means of a Tectra Gmbh ion gun with an 800 eV Ar + beam (gas purity N5.0) at a pressure of 4.0 × 10^{-4} mbar. The ion beam direction forms a −30° angle with respect to the glass surface normal, and the ion fluence corresponds to 1.4 × 10^{19} ions/cm^2. The sample holder is heated to a fixed temperature of about 680 K during the sputtering process by a fire rod heater.

After the IBS experiment, Au stripes are confined either on the long or short facets of the glass nanorippled asymmetric saw-tooth profile by grazing angle thermal deposition. Au is deposited on the long rippled facets (tilted at θ_{facets} = 35°) by selecting a $\theta_{Au\ beam}$ = 55° Au beam angle with respect to the flat sample surface normal. The long facets are thus illuminated by the Au beam at 20° local angle while the short facets on the other side of the ridge are completely shadowed. Similarly, Au stripes are confined on the short ripple facets (tilted at θ_{facets} = −45°) by selecting a $\theta_{Au\ beam}$ = −65° Au beam direction which again forms a 20° local angle with respect to the local facet surface normal. The thickness of the Au stripes h is controlled by means of a calibrated quartz microbalance considering the Au thickness deposited on a flat substrate (h_0) by basic trigonometric arguments by the relation $h = h_0 \times \cos(|\theta_{Au\ beam} - \theta_{facet}|)$. The Au deposition rate corresponds to about 1 Å/s for all experiments. The width w of the Au stripes is fixed by the facet choice and corresponds to about 120 nm for the long facets and 80 for the short ones.

TiO_2 layers have been grown with a custom-made RF sputtering system using a 2″ titanium target. The reactive RF sputtering experiment is run in a mixed argon and oxygen atmosphere at a power P = 10 W and sample−target distance d = 8.5 cm. The TiO_2 layer thickness was monitored with a calibrated quartz microbalance. The TiO_2 thin film has been characterized by both optical transmission and Raman measurements.

Morphological Characterization. AFM topographies of the nanorippled glass surface have been acquired by means of a Nanosurf S Mobile microscope operating in noncontact mode. The analysis of AFM images has been performed with WsXM software.[68] Top-view SEM images have been acquired with a thermionic Hitachi VP-SEM SU3500.

Optical Characterization. Normal-incidence extinction spectra of nanorippled glass−Au stripes and MB solutions are acquired by employing a fiber coupled compensated halogen-deuterium lamp (DH-2000-BAL, Mikropak) and a Vis−NIR spectrometer (HR4000, Oceans Optics) operating in the 300−1100 nm spectral range. The macroscopic spot size diameter is about 1 mm. For linearly polarized measurements, a Thorlabs Glen−Thompson polarizer has been used. A flat, bare glass is used as reference in the case of nanorippled Au stripe measurements performed in air. An empty cuvette is used as reference in the case of MB solution measurements. A MB-filled cuvette with a flat, bare glass inside is used as reference in the case of nanorippled Au NSs measurements in MB.

Photocatalysis Experiments. MB solutions are prepared at a fixed concentration of C_0 = 1.3 × 10^{-5} mol L^{-1} by diluting MB

https://doi.org/10.1021/acsanm.1c04087
ACS Appl. Nano Mater. 2022, 5, 3470−3479

powder in mQ water. MB concentration is estimated optically by measuring the adimensional solution absorbance $A = -\log(T)$, where T is the solution transmittance, and using the Beer Lambert law resolved for the concentration $C = Ad^{-1}\varepsilon^{-1}$, where d is the optical path expressed in cm and ε is the molar absorption coefficient, for which we used the literature value of 7.5×10^5 L mol^{-1} cm^{-1}. Two quartz cuvettes with a 1 cm side square internal section are filled with 2 mL of MB solution and a little magnetic stirrer. The cuvettes are covered with parafilm to avoid solvent evaporation and left stirring at room temperature for 1 h. A nanorippled glass−Au stripe sample is then put inside one of the cuvettes. The sample is cut to perfectly fit the width of the cuvette and level of the MB solution inside it. Both solutions are left stirring for another hour to reach a complete surface absorption/desorption equilibrium before exposure (see Figure S3).

After this initial procedure, both cuvettes are illuminated with a Newport TLS130B-300X tunable light source, equipped with a 300 W Xenon arc lamp, a CS130B monochromator, and a 1 in. output flange. The monochromatized beam (±25 nm of bandwidth) passes through a Thorlabs WP25M-UB ultra broad band wire grid polarizer before reaching the cuvettes, so that the electric field oscillates orthogonally to the Au NSs facing the beam (see the scheme in Figure 3a). The cuvettes are put one beside the other at about 40 cm of distance from the lamp output flange so that the beam uniformly illuminates both of them. The average beam power density at the cuvette location is measured with a Newport 818-UV optical power detector connected to a Newport 1919-R optical power meter. The source power is tuned so that the power density is equal to 2 W cm^{-2} for all the experiments performed at different monochromatization wavelengths. Every 30 min, the position of the cuvettes is swapped for better exposure uniformity. At regular intervals of photon dose, the absorbance of both solutions is measured using the extinction setup described in the previous subchapter and a custom-made cuvette holder. The absorbance evolution of the MB solution containing the sample is discussed and compared to the reference one (solution with no sample) for different exposure wavelengths in the Results and Discussion section.

■ ASSOCIATED CONTENT

Supporting Information

The Supporting Information is available free of charge at https://pubs.acs.org/doi/10.1021/acsanm.1c04087.

2D autocorrelation function, extinction spectra, normalized absorption peak, picture of the sample inside the MB solution, convolution integral, SEM images, reflectance spectrum, polarized TM total reflectance, and normalized concentration (PDF)

■ AUTHOR INFORMATION

Corresponding Author

Francesco Buatier de Mongeot − *Dipartimento di Fisica, Università di Genova, Genova I-16146, Italy;* orcid.org/0000-0002-8144-701X; Email: buatier@fisica.unige.it

Authors

Matteo Barelli − *Dipartimento di Fisica, Università di Genova, Genova I-16146, Italy;* Present Address: Photonic Nanomaterials Lab, Istituto Italiano di Tecnologia (IIT), 16163 Genova, Italy; orcid.org/0000-0002-3960-7921

Giulio Ferrando − *Dipartimento di Fisica, Università di Genova, Genova I-16146, Italy*

Maria Caterina Giordano − *Dipartimento di Fisica, Università di Genova, Genova I-16146, Italy;* orcid.org/0000-0002-9757-4339

Complete contact information is available at: https://pubs.acs.org/10.1021/acsanm.1c04087

Author Contributions

M.B. and F.B. conceived the idea. M.B., G.F., and M.C.G. performed the experiments and conceived the experimental setup. All the authors contributed to the writing of the manuscript. F.B. also supervised the project.

Notes

The authors declare no competing financial interest.

■ ACKNOWLEDGMENTS

F.B.d.M. and M.C.G. acknowledge financial support by Ministero dell'Università e della Ricerca, within the project "Dipartimento di Eccellenza 2018-2022" art. 1, c. 314-337, Legge 232/2016. M.C.G. acknowledges financial support by Ministero degli Affari Esteri e della Cooperazione Internazionale within the bilateral project Italy-Vietnam 2021-2023 "Large-area 2D/plasmonic heterostructures for photocatalysis and energy storage (H2D)". F.B.d.M. and M.C.G. acknowledge support by Università degli Studi di Genova within the project "Fondi di Ricerca di Ateneo" and BIPE2020.

■ REFERENCES

(1) Gramotnev, D. K.; Bozhevolnyi, S. I. Plasmonics beyond the Diffraction Limit. *Nat. Photonics* **2010**, *4*, 83−91.

(2) Muhlschlegel, P. Resonant Optical Antennas. *Science* **2005**, *308*, 1607−1609.

(3) Ciraci, C.; Hill, R. T.; Mock, J. J.; Urzhumov, Y.; Fernandez-Dominguez, A. I.; Maier, S. A.; Pendry, J. B.; Chilkoti, A.; Smith, D. R. Probing the Ultimate Limits of Plasmonic Enhancement. *Science* **2012**, *337*, 1072−1074.

(4) Fernández-Domínguez, A. I.; García-Vidal, F. J.; Martín-Moreno, L. Unrelenting Plasmons. *Nat. Photonics* **2017**, *11*, 8−10.

(5) Maier, S. A. *Plasmonics: Fundamentals and Applications*; Springer US: New York, NY, 2007.

(6) Zayats, A. V.; Smolyaninov, I. I.; Maradudin, A. A. Nano-Optics of Surface Plasmon Polaritons. *Phys. Rep.* **2005**, *408*, 131−314.

(7) Anker, J. N.; Hall, W. P.; Lyandres, O.; Shah, N. C.; Zhao, J.; Van Duyne, R. P. Biosensing with Plasmonic Nanosensors. *Nat. Mater.* **2008**, *7*, 442−453.

(8) Lal, S.; Link, S.; Halas, N. J. Nano-Optics from Sensing to Waveguiding. *Nat. Photonics* **2007**, *1*, 641−648.

(9) Brown, L. V.; Yang, X.; Zhao, K.; Zheng, B. Y.; Nordlander, P.; Halas, N. J. Fan-Shaped Gold Nanoantennas above Reflective Substrates for Surface-Enhanced Infrared Absorption (SEIRA). *Nano Lett.* **2015**, *15*, 1272−1280.

(10) Kristensen, A.; Yang, J. K. W.; Bozhevolnyi, S. I.; Link, S.; Nordlander, P.; Halas, N. J.; Mortensen, N. A. Plasmonic Colour Generation. *Nat. Rev. Mater.* **2017**, *2*, 16088.

(11) Atwater, H. A.; Polman, A. Plasmonics for Improved Photovoltaic Devices. *Nat. Mater.* **2010**, *9*, 205−213.

(12) Zhou, N.; López-Puente, V.; Wang, Q.; Polavarapu, L.; Pastoriza-Santos, I.; Xu, Q.-H. Plasmon-Enhanced Light Harvesting: Applications in Enhanced Photocatalysis, Photodynamic Therapy and Photovoltaics. *RSC Adv.* **2015**, *5*, 29076−29097.

(13) Langer, J.; Jimenez de Aberasturi, D.; Aizpurua, J.; Alvarez-Puebla, R. A.; Auguié, B.; Baumberg, J. J.; Bazan, G. C.; Bell, S. E. J.; Boisen, A.; Brolo, A. G.; Choo, J.; Cialla-May, D.; Deckert, V.; Fabris, L.; Faulds, K.; García de Abajo, F. J.; Goodacre, R.; Graham, D.; Haes, A. J.; Haynes, C. L.; Huck, C.; Itoh, T.; Käll, M.; Kneipp, J.; Kotov, N. A.; Kuang, H.; Le Ru, E. C.; Lee, H. K.; Li, J.-F.; Ling, X. Y.; Maier, S. A.; Mayerhöfer, T.; Moskovits, M.; Murakoshi, K.; Nam, J.-M.; Nie, S.; Ozaki, Y.; Pastoriza-Santos, I.; Perez-Juste, J.; Popp, J.; Pucci, A.; Reich, S.; Ren, B.; Schatz, G. C.; Shegai, T.; Schlücker, S.; Tay, L.-L.; Thomas, K. G.; Tian, Z.-Q.; Van Duyne, R. P.; Vo-Dinh, T.; Wang, Y.; Willets, K. A.; Xu, C.; Xu, H.; Xu, Y.; Yamamoto, Y. S.; Zhao, B.; Liz-Marzán, L. M. Present and Future of Surface-Enhanced Raman Scattering. *ACS Nano* **2020**, *14*, 28−117.

(14) Ni, X.; Wong, Z. J.; Mrejen, M.; Wang, Y.; Zhang, X. An Ultrathin Invisibility Skin Cloak for Visible Light. *Science* **2015**, *349*, 1310−1314.
(15) Yuan, X.; He, Z.; Ye, X.; Chen, M.; Li, Y.; Li, W.; Zhang, R.; Huang, Y.; Liu, C.; Cheng, X.; Fang, D. Invisible Electromagnetic Huygens' Metasurface Operational in Wide Frequency Band and Its Experimental Validation. *IEEE Trans. Antennas Propag.* **2021**, *69*, 3341−3348.
(16) Brongersma, M. L.; Halas, N. J.; Nordlander, P. Plasmon-Induced Hot Carrier Science and Technology. *Nat. Nanotechnol.* **2015**, *10*, 25−34.
(17) Hartland, G. V.; Besteiro, L. V.; Johns, P.; Govorov, A. O. What's so Hot about Electrons in Metal Nanoparticles? *ACS Energy Lett.* **2017**, *2*, 1641−1653.
(18) Clavero, C. Plasmon-Induced Hot-Electron Generation at Nanoparticle/Metal-Oxide Interfaces for Photovoltaic and Photocatalytic Devices. *Nat. Photonics* **2014**, *8*, 95−103.
(19) Knight, M. W.; Sobhani, H.; Nordlander, P.; Halas, N. J. Photodetection with Active Optical Antennas. *Science* **2011**, *332*, 702−704.
(20) Mascaretti, L.; Dutta, A.; Kment, Š.; Shalaev, V. M.; Boltasseva, A.; Zbořil, R.; Naldoni, A. Plasmon-Enhanced Photoelectrochemical Water Splitting for Efficient Renewable Energy Storage. *Adv. Mater.* **2019**, *31*, No. 1805513.
(21) Linic, S.; Chavez, S.; Elias, R. Flow and Extraction of Energy and Charge Carriers in Hybrid Plasmonic Nanostructures. *Nat. Mater.* **2021**, *20*, 916−924.
(22) Kale, M. J.; Avanesian, T.; Christopher, P. Direct Photocatalysis by Plasmonic Nanostructures. *ACS Catal.* **2014**, *4*, 116−128.
(23) Zhang, Y.; He, S.; Guo, W.; Hu, Y.; Huang, J.; Mulcahy, J. R.; Wei, W. D. Surface-Plasmon-Driven Hot Electron Photochemistry. *Chem. Rev.* **2018**, *118*, 2927−2954.
(24) Kundu, S.; Patra, A. Nanoscale Strategies for Light Harvesting. *Chem. Rev.* **2017**, *117*, 712−757.
(25) DuChene, J. S.; Tagliabue, G.; Welch, A. J.; Cheng, W.-H.; Atwater, H. A. Hot Hole Collection and Photoelectrochemical CO_2 Reduction with Plasmonic Au/p-GaN Photocathodes. *Nano Lett.* **2018**, *18*, 2545−2550.
(26) Cortés, E.; Xie, W.; Cambiasso, J.; Jermyn, A. S.; Sundararaman, R.; Narang, P.; Schlücker, S.; Maier, S. A. Plasmonic Hot Electron Transport Drives Nano-Localized Chemistry. *Nat. Commun.* **2017**, *8*, 14880.
(27) Zhang, J.; Langille, M. R.; Mirkin, C. A. Synthesis of Silver Nanorods by Low Energy Excitation of Spherical Plasmonic Seeds. *Nano Lett.* **2011**, *11*, 2495−2498.
(28) Brus, L. Growing Gold Nanoprisms with Light. *Nat. Mater.* **2016**, *15*, 824−825.
(29) Mukherjee, S.; Libisch, F.; Large, N.; Neumann, O.; Brown, L. V.; Cheng, J.; Lassiter, J. B.; Carter, E. A.; Nordlander, P.; Halas, N. J. Hot Electrons Do the Impossible: Plasmon-Induced Dissociation of H_2 on Au. *Nano Lett.* **2013**, *13*, 240−247.
(30) Naldoni, A.; Guler, U.; Wang, Z.; Marelli, M.; Malara, F.; Meng, X.; Besteiro, L. V.; Govorov, A. O.; Kildishev, A. V.; Boltasseva, A.; Shalaev, V. M. Broadband Hot-Electron Collection for Solar Water Splitting with Plasmonic Titanium Nitride. *Adv. Opt. Mater.* **2017**, *5*, No. 1601031.
(31) Wang, F.; Li, C.; Chen, H.; Jiang, R.; Sun, L.-D.; Li, Q.; Wang, J.; Yu, J. C.; Yan, C.-H. Plasmonic Harvesting of Light Energy for Suzuki Coupling Reactions. *J. Am. Chem. Soc.* **2013**, *135*, 5588−5601.
(32) Salmón-Gamboa, J. U.; Romero-Gómez, M.; Roth, D. J.; Barber, M. J.; Wang, P.; Fairclough, S. M.; Nasir, M. E.; Krasavin, A. V.; Dickson, W.; Zayats, A. V. Optimizing Hot Carrier Effects in Pt-Decorated Plasmonic Heterostructures. *Faraday Discuss.* **2019**, *214*, 387−397.
(33) Liu, T.; Li, Y. Plasmonic Solar Desalination. *Nat. Photonics* **2016**, *10*, 361−362.
(34) *Surface-Enhanced Raman Scattering*; Kneipp, K.; Moskovits, M.; Kneipp, H., Eds.; Topics in Applied Physics; Springer: Berlin, Heidelberg, 2006; Vol. *103*.
(35) Gao, L.; Liu, R.; Gao, F.; Wang, Y.; Jiang, X.; Gao, X. Plasmon-Mediated Generation of Reactive Oxygen Species from Near-Infrared Light Excited Gold Nanocages for Photodynamic Therapy *in Vitro*. *ACS Nano* **2014**, *8*, 7260−7271.
(36) Wen, T.; Zhang, H.; Chong, Y.; Wamer, W. G.; Yin, J.-J.; Wu, X. Probing Hydroxyl Radical Generation from H2O2 upon Plasmon Excitation of Gold Nanorods Using Electron Spin Resonance: Molecular Oxygen-Mediated Activation. *Nano Res.* **2016**, *9*, 1663−1673.
(37) Labouret, T.; Audibert, J.-F.; Pansu, R. B.; Palpant, B. Plasmon-Assisted Production of Reactive Oxygen Species by Single Gold Nanorods. *Small* **2015**, *11*, 4475−4479.
(38) Robatjazi, H.; Bahauddin, S. M.; Doiron, C.; Thomann, I. Direct Plasmon-Driven Photoelectrocatalysis. *Nano Lett.* **2015**, *15*, 6155−6161.
(39) Liang, W.; Sun, Y.; Liang, Z.; Li, D.; Wang, Y.; Qin, W.; Jiang, L. Plasmonic Nanoparticle Film for Low-Power NIR-Enhanced Photocatalytic Reaction. *ACS Appl. Mater. Interfaces* **2020**, *12*, 16753−16761.
(40) Wang, C.; Nie, X.-G.; Shi, Y.; Zhou, Y.; Xu, J.-J.; Xia, X.-H.; Chen, H.-Y. Direct Plasmon-Accelerated Electrochemical Reaction on Gold Nanoparticles. *ACS Nano* **2017**, *11*, 5897−5905.
(41) Zheng, Z.; Tachikawa, T.; Majima, T. Single-Particle Study of Pt-Modified Au Nanorods for Plasmon-Enhanced Hydrogen Generation in Visible to Near-Infrared Region. *J. Am. Chem. Soc.* **2014**, *136*, 6870−6873.
(42) Shi, X.; Ueno, K.; Oshikiri, T.; Sun, Q.; Sasaki, K.; Misawa, H. Enhanced Water Splitting under Modal Strong Coupling Conditions. *Nat. Nanotechnol.* **2018**, *13*, 953−958.
(43) Zhang, C.; Zhao, H.; Zhou, L.; Schlather, A. E.; Dong, L.; McClain, M. J.; Swearer, D. F.; Nordlander, P.; Halas, N. J. Al−Pd Nanodisk Heterodimers as Antenna−Reactor Photocatalysts. *Nano Lett.* **2016**, *16*, 6677−6682.
(44) Mubeen, S.; Lee, J.; Singh, N.; Krämer, S.; Stucky, G. D.; Moskovits, M. An Autonomous Photosynthetic Device in Which All Charge Carriers Derive from Surface Plasmons. *Nat. Nanotechnol.* **2013**, *8*, 247−251.
(45) Wu, B.; Liu, D.; Mubeen, S.; Chuong, T. T.; Moskovits, M.; Stucky, G. D. Anisotropic Growth of TiO_2 onto Gold Nanorods for Plasmon-Enhanced Hydrogen Production from Water Reduction. *J. Am. Chem. Soc.* **2016**, *138*, 1114−1117.
(46) Tan, S.; Argondizzo, A.; Ren, J.; Liu, L.; Zhao, J.; Petek, H. Plasmonic Coupling at a Metal/Semiconductor Interface. *Nat. Photonics* **2017**, *11*, 806−812.
(47) Giordano, M. C.; de Mongeot, F. B. Anisotropic Nanoscale Wrinkling in Solid-State Substrates. *Adv. Mater.* **2018**, *30*, No. 1801840.
(48) Repetto, D.; Giordano, M. C.; Foti, A.; Gucciardi, P. G.; Mennucci, C.; Buatier de Mongeot, F. SERS Amplification by Ultra-Dense Plasmonic Arrays on Self-Organized PDMS Templates. *Appl. Surf. Sci.* **2018**, *446*, 83−91.
(49) Barelli, M.; Giordano, M. C.; Gucciardi, P. G.; Buatier de Mongeot, F. Self-Organized Nanogratings for Large-Area Surface Plasmon Polariton Excitation and Surface-Enhanced Raman Spectroscopy Sensing. *ACS Appl. Nano Mater.* **2020**, *3*, 8784−8793.
(50) Barabási, A.-L.; Stanley, H. E. *Fractal Concepts in Surface Growth*, 1st ed.; Cambridge University Press, 1995
(51) Cuerno, R.; Barabási, A.-L. Dynamic Scaling of Ion-Sputtered Surfaces. *Phys. Rev. Lett.* **1995**, *74*, 4746−4749.
(52) Costantini, G.; Buatier de Mongeot, F.; Boragno, C.; Valbusa, U. Is Ion Sputtering Always a "Negative Homoepitaxial Deposition"? *Phys. Rev. Lett.* **2001**, *86*, 838−841.
(53) Bradley, R. M.; Harper, J. M. E. Theory of Ripple Topography Induced by Ion Bombardment. *J. Vac. Sci. Technol., A* **1988**, *6*, 2390−2395.
(54) Giordano, M. C.; di Sacco, F.; Barelli, M.; Portale, G.; Buatier de Mongeot, F. Self-Organized Tailoring of Faceted Glass Nanowrinkles for Organic Nanoelectronics. *ACS Appl. Nano Mater.* **2021**, *4*, 1940−1950.

https://doi.org/10.1021/acsanm.1c04087
ACS Appl. Nano Mater. 2022, 5, 3470−3479

(55) Giordano, M. C.; Repetto, D.; Mennucci, C.; Carrara, A.; de Mongeot, F. B. Template-Assisted Growth of Transparent Plasmonic Nanowire Electrodes. *Nanotechnology* **2016**, *27*, No. 495201.
(56) Mennucci, C.; Del Sorbo, S.; Pirotta, S.; Galli, M.; Andreani, L. C.; Martella, C.; Giordano, M. C.; Buatier de Mongeot, F. Light Scattering Properties of Self-Organized Nanostructured Substrates for Thin-Film Solar Cells. *Nanotechnology* **2018**, *29*, 355301.
(57) Barelli, M.; Mazzanti, A.; Giordano, M. C.; Della Valle, G.; Buatier de Mongeot, F. Color Routing via Cross-Polarized Detuned Plasmonic Nanoantennas in Large-Area Metasurfaces. *Nano Lett.* **2020**, *20*, 4121−4128.
(58) Giordano, M. C.; Tzschoppe, M.; Barelli, M.; Vogt, J.; Huck, C.; Canepa, F.; Pucci, A.; Buatier de Mongeot, F. Self-Organized Nanorod Arrays for Large-Area Surface-Enhanced Infrared Absorption. *ACS Appl. Mater. Interfaces* **2020**, *12*, 11155−11162.
(59) Giordano, M. C.; Longhi, S.; Barelli, M.; Mazzanti, A.; Buatier de Mongeot, F.; Della Valle, G. Plasmon Hybridization Engineering in Self-Organized Anisotropic Metasurfaces. *Nano Res.* **2018**, *11*, 3943−3956.
(60) Muskens, O.; Christofilos, D.; Fatti, N. D.; Vallée, F. Optical Response of a Single Noble Metal Nanoparticle. *J. Opt. A: Pure Appl. Opt.* **2006**, *8*, S264−S272.
(61) Atkins, P. W.; De Paula, J.; Keeler, J. *Atkins' Physical Chemistry: Thermodynamics and Kinetics*, 11th ed.; Oxford University Press: Oxford, United Kingdom, 2018.
(62) Sáenz-Trevizo, A.; Pizá-Ruiz, P.; Chávez-Flores, D.; Ogaz-Parada, J.; Amézaga-Madrid, P.; Vega-Ríos, A.; Miki-Yoshida, M. On the Discoloration of Methylene Blue by Visible Light. *J. Fluoresc.* **2019**, *29*, 15−25.
(63) Li, K.; Hogan, N. J.; Kale, M. J.; Halas, N. J.; Nordlander, P.; Christopher, P. Balancing Near-Field Enhancement, Absorption, and Scattering for Effective Antenna−Reactor Plasmonic Photocatalysis. *Nano Lett.* **2017**, *17*, 3710−3717.
(64) Yuan, L.; Lou, M.; Clark, B. D.; Lou, M.; Zhou, L.; Tian, S.; Jacobson, C. R.; Nordlander, P.; Halas, N. J. Morphology-Dependent Reactivity of a Plasmonic Photocatalyst. *ACS Nano* **2020**, *14*, 12054−12063.
(65) Luttrell, T.; Halpegamage, S.; Tao, J.; Kramer, A.; Sutter, E.; Batzill, M. Why Is Anatase a Better Photocatalyst than Rutile? - Model Studies on Epitaxial TiO2 Films. *Sci. Rep.* **2015**, *4*, 4043.
(66) Debu, D. T.; Ghosh, P. K.; French, D.; Herzog, J. B. Surface Plasmon Damping Effects Due to Ti Adhesion Layer in Individual Gold Nanodisks. *Opt. Mater. Express* **2017**, *7*, 73.
(67) Dmitriev, A.; Pakizeh, T.; Käll, M.; Sutherland, D. S. Gold−Silica−Gold Nanosandwiches: Tunable Bimodal Plasmonic Resonators. *Small* **2007**, *3*, 294−299.
(68) Horcas, I.; Fernández, R.; Gómez-Rodríguez, J. M.; Colchero, J.; Gómez-Herrero, J.; Baro, A. M. WSXM : A Software for Scanning Probe Microscopy and a Tool for Nanotechnology. *Rev. Sci. Instrum.* **2007**, *78*, 013705.

https://doi.org/10.1021/acsanm.1c04087
ACS Appl. Nano Mater. 2022, 5, 3470−3479